ELSEVIER

Contents lists available at ScienceDirect

Corrosion Communications

journal homepage: www.elsevier.com/locate/corcom



Research Article

HiPIMS-deposited Cr_xN coatings for marine applications: Controllable microstructure and tribocorrosion behavior



Xiaohui Zhou^{a,c}, Hong Du^a, Guanshui Ma^a, Zhenyu Wang^a, Wei Yang^a, Kazuhito Nishimura^a, Peng Guo^a, Aiying Wang^{a,b}, Peiling Ke^{a,b,*}

- ^a State Key Laboratory of Advanced Marine Materials, Zhejiang Key Laboratory of Extreme-environmental Material Surfaces and Interfaces, Ningbo Institute of Materials Technology and Engineering, Chinese Academy of Sciences, Ningbo 315201, China
- ^b Center of Materials Science and Optoelectronics Engineering, University of Chinese Academy of Sciences, Beijing 100049, China
- ^c School of Physical Science and Technology, ShanghaiTech University, Shanghai 201210, China

ARTICLE INFO

Article history: Received 15 April 2024 Received in revised form 17 May 2024 Accepted 21 May 2024 Available online 13 July 2025

Keywords: CrN coating HiPIMS Microstructure Tribocorrosion

ABSTRACT

A series of Cr_xN coatings (x=1 or 2) were fabricated on the 431 stainless steel using a high power impulse magnetron sputtering (HiPIMS), with varying $Ar:N_2$ ratios. The microstructure and phase structures of the resulting coatings were characterized using multiple microscopic techniques. Tribocorrosion behavior was evaluated through ball-on-disk friction and wear tests in an artificial seawater environment. The results demonstrated that the coating prepared with a $Ar:N_2=5:2$ gas mixture exhibited the best tribocorrosion performance, featuring the lowest wear depth and wear rate. This was attributed to its denser dual-phase structure composed of CrN and Cr_2N .

© 2025 The Authors. Published by Elsevier B.V. on behalf of Institute of Metal Research, Chinese Academy of Sciences.

This is an open access article under the CC BY-NC-ND license (http://creativecommons.org/licenses/by-nc-nd/4.0/)

1. Introduction

For mechanical transmission components like submarine stern shafts, support bearings, and gears operating in the harsh ocean environments, tribocorrosion—the combined effect of saline-water corrosion and mechanical friction—poses a major challenge. This synergistic degradation significantly compromises component integrity [1]. 431 stainless steel is widely used in the maritime industry due to its excellent corrosion resistance, along with high tensile and yield strength [2]. In addition, coatings fabricated on alloy surfaces using advanced physical vapor deposition (PVD) techniques offer enhanced properties such as high hardness [3,4], excellent chemical stability [5], and superior wear resistance [6], making them a focal point of extensive research.

Among these, CrN coating represents a class of metal nitrides well known for their high hardness, excellent wear resistance, and superior corrosion protection. They are extensively used in applications such as cutting tools, molds, and stamping dies [7–11]. CrN coatings exhibit better corrosion resistance than TiN and TiAlN coatings in 3.5 wt.% NaCl solution [12]. Additionally, CrN can form Cr-rich oxides during friction, which act as solid lubricants to reduce the friction coefficient [13].

High power impulse magnetron sputtering (HiPIMS) has notable advantages over conventional direct current (DC) magnetron sputtering, offering higher ionization rates and ion flux, which lead to improved coating structure and enhanced properties [14,15]. Tranca et al. [16] compared the CrN coatings deposited by DC and HiPIMS on Si substrates and found that HiPIMS-produced coatings exhibited higher Young's modulus (240–250 GPa) and stiffness (125–132 N/m).

The composition and structure of $\mathrm{Cr_xN}$ largely depend on the nitrogen flow. Zhang et al. [17] reported that varying nitrogen flow significantly alters the preferred crystal orientation of $\mathrm{Cr_xN}$ coatings, although hardness and adhesion do not show a direct correlation. In contrast, Chen et al. [18] found that higher nitrogen partial pressures, which promote CrN phase formation, increase coating hardness but may reduce adhesion. Prior studies [19,20] have shown that a gas ratio of $\mathrm{Ar:N_2}{=}3:1$ produces $\mathrm{Cr}{+}\mathrm{Cr_2N}$ phases, while a 1:1 ratio results in pure CrN. These differing structures lead to distinct properties: under the same thickness, $\mathrm{Cr_2N}$ coatings have higher hardness and Young's modulus than CrN, whereas CrN coatings offer better oxidation resistance and lower friction coefficients. Parameters such as crystal preferred orientation, grain size and phase structure, significantly influence the coatings' corrosion and wear resistance [21].

^{*} Corresponding author.

E-mail address: kepl@nimte.ac.cn (P. Ke).

Table 1 Chemical composition (g L^{-1}) of artificial seawater.

NaCl	$\mathrm{Na_2SO_4}$	MgCl_2	CaCl_2	${\rm SrCl}_2$	KCl	$NaHCO_3$	KBr	H_3BO_3	NaF
24.53	4.09	5.20	1.16	0.025	0.695	0.201	0.101	0.027	0.003

However, comprehensive studies on the tribocorrosion and mechanical properties of dual-phase CrN/Cr_2N coatings in simulated seawater environments remain limited. In this study, Cr_xN coatings with varying N_2 contents were deposited using HiPIMS. Their tribocorrosion behavior in artificial seawater was systematically investigated to provide theoretical insights and experimental evidence for the development of nitrogen-based marine protective coatings.

2. Experimental

2.1. Coating preparation

The $\rm Cr_x N$ coatings were deposited on the polished 431 stainless steels ($\rm \Phi 17~mm \times 3~mm$) and P-type (100) Si wafers by HiPIMS. The coating deposition equipment was configured with a pure chromium target (99.9%, mass fraction) in the size of 400 mm \times 100 mm \times 5 mm, and a linear ion source (LIS). Prior to deposition, all substrates were continuously ultrasonically cleaned in acetone and ethanol. The distance from the base to the target was 10 cm and the vacuum of the vacuum chamber was drained to approximately 2.67 \times 10 $^{-3}$ Pa. All substrates were etched and pre-cleaned with an Ar $^+$ source for 40 min and with a negative bias of $-100~\rm V$.

During the coating process, the Cr layer was deposited by HiPIMS at 2500 W power and 50 mL/min Ar for 4 min, and then Ar and $\rm N_2$ were introduced at the ratios of 60:20, 50:20 and 40:40 respectively. The gas pressure reached 1.50 Pa, in which $\rm N_2$ was introduced from the linear ionization source and the Ar magnetron sputtering source. In the process of film preparation, the power of HiPIMS was 2500 W, and the current of linear ion source was 0.15 A. A negative bias voltage of 100 V is applied to the substrate by DC pulse bias power supply and the deposition time of $\rm Cr_x N$ film was 120 min.

2.2. Characterization

Phase structures were studied by an X-ray diffractometer (XRD, Bruker D8 X-ray facility) using Cu K_{α} radiation ($\lambda = 0.154$ nm) at 40 kV, 40 mA and a grazing incidence angle of 2°. The scanning angle was $20^{\circ}-90^{\circ}$, the scanning speed was $4^{\circ}/\text{min}$, and the step size was 0.02. The cross-sectional images of coating on Si substrate and wear track morphology of the coating were observed by a field emission scanning electron microscope (SEM, Hitachi S4800), and the surface element composition of the coating was determined according to the peak area ratios of X-ray photoelectron spectroscopy (XPS, AXIS SUPRA). In addition, it characterized the corrosion resistance and mechanical properties of the coating. The traditional three-electrode electrochemical cell was used for electrochemical measurement on the 600 + (Gamry) electrochemical workstation, in which Cr_xN was used as the working electrode, saturated calomel as the reference electrode and platinum plate as the counter electrode. Prior to initiating all corrosion tests, an open circuit potential (OCP) measurement was conducted for 60 min. Once the OCP had gradually stabilized, the corresponding scanning procedure was subsequently performed. The experiment was conducted at ambient temperature ((25 \pm 1) °C) and in artificial seawater prepared according to ASTM D1141–98 [22]. The chemical composition of artificial seawater is listed in Table 1. The potential dynamic current potential curve was recorded at a scanning rate of 3 mV/s.

Nano indentation (Nano Indenter) was used to measure hardness (H) and elastic modulus (E) by the continuous stiffness method. The pressing depth was controlled to 2 μ m. The selection depth of characteristic values H and E is about 200 nm to avoid the effect caused by the substrate.

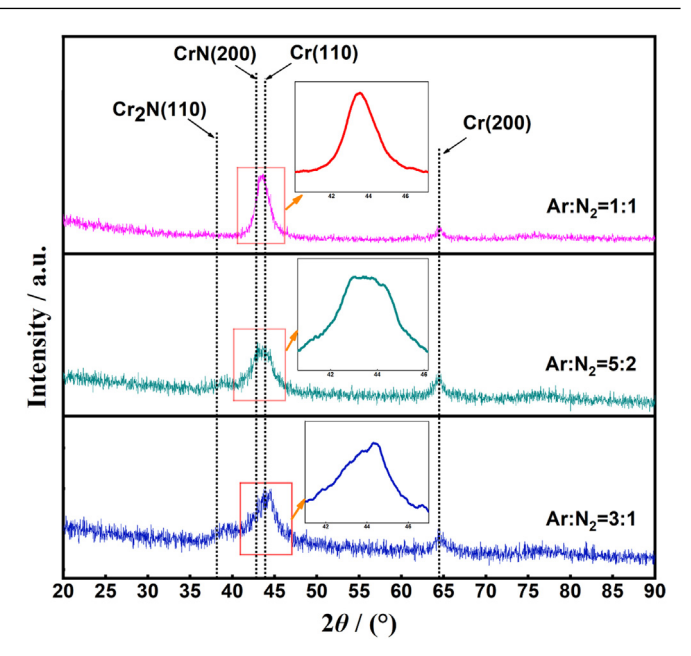


Fig. 1. XRD pattern of Cr_xN coatings with different $Ar:N_2$ deposited on 431 steel substrates.

Ten dents were made on each coating sample, and the average H and E were evaluated from the load-displacement curve. The atomic force microscope (AFM, 3100v) was used to measure the surface roughness (Ra) of the Cr_xN coatings.

2.3. Tribocorrosion test

The wear test was carried out on a UMT-3MT Tribometer (CETR). Under the conditions of room temperature of (25±1) °C and relative humidity of (70±5)%, $\rm Si_3N_4$ ball slides on $\rm Cr_xN$ coatings in ball surface reciprocating motion mode. The diameter of $\rm Si_3N_4$ ball is 3 mm, and the test is carried out in artificial seawater prepared according to ASTM D1141–98 [22]. In order to evaluate the friction and wear characteristics of sliding parts, a sliding speed of 300 r/min, a constant normal load of 3 N and a sliding stroke of 5 mm were used in the test, and the friction coefficient was continuously recorded during the test. Before, during and after the sliding tests, OCP was monitored and recorded to investigate the tribocorrosion behavior.

The track depth in the wear mark is measured by the profiler (alpha step 1q). The wear rate (*W*) obtained after the tribocorrosion test can be calculated according to the classical wear equation [23]:

$$W = V/(F \times L) \tag{1}$$

where F is the applied normal load in N, V is the wear loss of the coating in mm³, and L is the total sliding distance in m.

3. Results and discussion

3.1. Phase and microstructure

Fig. 1 shows X-ray diffraction patterns of Cr_xN deposited on 431 steel substrates using different $Ar:N_2$ (3:1, 5:2, 1:1). For the $Ar:N_2$ =3:1 condition, peaks at 44.3° and 37.8° corresponding to Cr (110) and Cr_2N (110), respectively, indicate that the coating primarily consists of Cr and Cr_2N

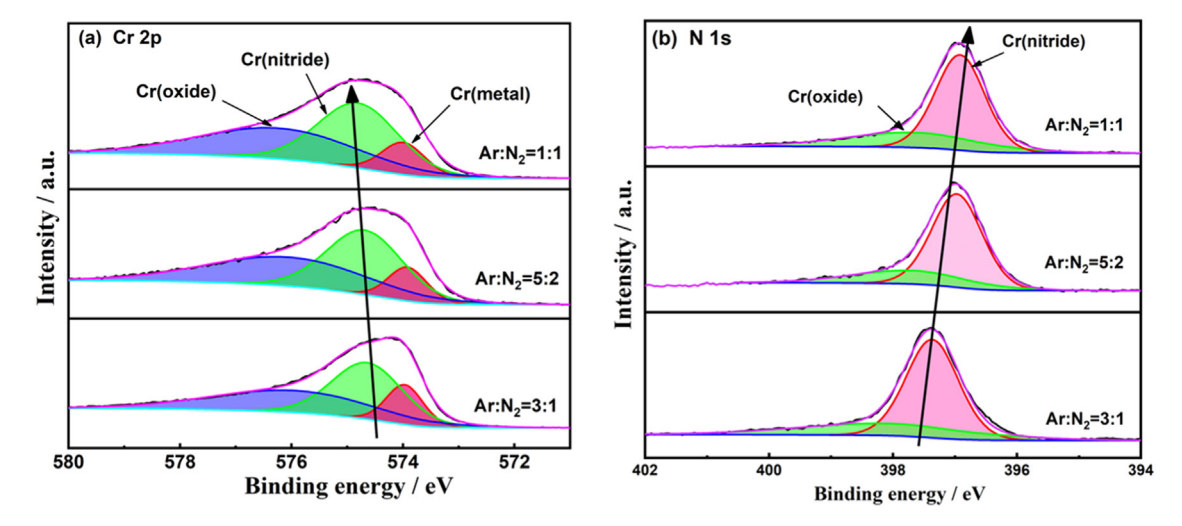


Fig. 2. Peak fitting for pristine CrN multilayer specimens: (a) Cr 2p, (b) N 1s.

phases. At $Ar:N_2 = 5:2$, the dominant peak shifts to 43.6° , corresponding to CrN, while the Cr_2N (110) peak at 37.8° remains, indicating a dual-phase composition of $CrN-Cr_2N$ [24]. The broadening of the peak in this case is attributed to the overlap between the Cr (110) and CrN (200) diffraction planes [25].

At the highest nitrogen flow (Ar: $N_2 = 1:1$), the Cr_2N (110) peak disappears, and the CrN (200) peak becomes predominant, confirming the formation of a primarily CrN phase with a (200) preferred orientation. These XRD results clearly demonstrate that the phase composition and structure of the Cr_xN coatings are strongly influenced by the nitrogen flow.

This trend can be explained by the ionization energies of the sputtering gases: argon (15.75 eV) and nitrogen (14.53 eV). At low nitrogen flow, the total reactive gas content is limited, leading to the preferential formation of Cr_2N due to limited nitrogen availability. As the nitrogen flow increases (Ar:N₂ = 1:1), more nitrogen ions are available to react with Cr atoms, promoting the formation of CrN as the dominant phase.

To further determine the composition and chemical state of the Cr_xN coatings, XPS was conducted, focusing on the Cr 2p3/2 and N 1s spectra. As shown in Fig. 2(a), the Cr 2p_{3/2} peaks at binding energies of 574, 574.5 and 576.1 eV correspond to metallic Cr, CrN [25,26] and Cr2N [27], respectively. A peak around (575.7 \pm 0.4) eV is also observed, which may result from Cr-O-N bond formation due to residual oxygen during deposition [28], making it difficult to distinguish between Cr₂N and chromium oxynitride (CrN_xO_y) phases. For the N 1s spectra, characteristic peaks are observed at 396.8 eV (CrN), 397.4 eV (Cr₂N), and (398.2 \pm 0.4) eV (chromium oxynitride) [29]. With increasing N₂ flow, the Cr $2p_{3/2}$ peak shifts toward higher binding energies, while the N 1s peak shifts toward lower binding energies. These shifts indicate enhanced formation of the CrN phase at higher nitrogen flow rates. This observation is consistent with the XRD results, confirming that a sufficient nitrogen supply promotes the formation of phase-pure CrN.

Fig. 3 shows the surface and cross-sectional micrographs of the $\mathrm{Cr_xN}$ coatings. At an $\mathrm{Ar:N_2}$ ratio of 3:1, the coating exhibits a well-defined columnar structure, with Cr clearly detectable in the cross-section (Fig. 3(a)). When the ratio is adjusted to 5:2, the columnar structure becomes significantly less distinct, and only a weak columnar structure is observed (Fig. 3(b)). This change is attributed to the competitive growth between $\mathrm{Cr_2N}$ (110) and CrN (200) crystallographic orientations. The interference between these two growth directions disrupts the formation of a uniform columnar structure [21]. However, at an $\mathrm{Ar:N_2}$ ratio of 1:1, a distinct columnar morphology reappears (Fig. 3(c)), due to the dominance of CrN (200) orientation.

 Cr_2N coatings generally exhibit a less pronounced columnar microstructure compared to the CrN coating, consistent with reports on magnetron-sputtered Cr_2N and CrN coatings [9,19,30]. Surface SEM images and roughness measurements for coatings prepared at $Ar:N_2$ ratios of 3:1, 5:2 and 1:1 are shown in Fig. 3(d, g), (e, h) and (f, i), respectively. The coating produced at 5:2 displays the smallest surface grains and the lowest Ra (0.256 nm), which is attributed to the interference between competing columnar growth directions in the dual-phase structure.

Fig. 4 shows TEM image and corresponding selected-area electron diffraction (SAED) pattern of the $\rm Cr_x N$ coating deposited at $\rm Ar: N_2 = 5:2$. The cross-sectional morphology reveals a clear columnar structure extending throughout the film. SAED pattern confirms the presence of CrN (111), (200) and $\rm Cr_2 N$ (211) phases. The diffuse nature of the diffraction rings suggests interfacial interference between the two phases during growth, further supporting the competitive growth mechanism identified in the XRD analysis.

Fig. 5(a) displays the characteristic columnar microstructure of the coating. High-resolution TEM in Fig. 5(b) reveals two distinct phase regions. IFFT analysis of area A (Fig. 5(c)) confirms the coexistence of [200] $_{\rm fcc}$ -CrN and [100] $_{\rm hcp}$ -Cr $_{\rm 2}$ N phases. IFFT images of regions B and C (Fig. 5(d, e)) display lattice fringes with spacings of 2.081 and 4.096 Å, corresponding to CrN (200) and Cr $_{\rm 2}$ N (100) planes, respectively. Among the fcc CrN planes, the (200) orientation has the lowest surface energy but requires substantial atomic diffusion. The high-energy plasma environment in HiPIMS enhances atomic mobility, promoting the development of (200)-oriented textures [31].

The competitive growth between CrN and Cr_2N phases results in mutually constrained columnar microstructures. This interphase interference leads to grain refinement, as the growing columnar crystals of each phase restrict and disrupt the development of one another.

The results demonstrate that variations in N_2 flow rate significantly influence the growth orientation of different valence compounds (CrN, Cr₂N, and Cr) within the coating. When the coating exhibits a dual-phase structure (Cr₂N/Cr or CrN/Cr₂N), the columnar growth is notably disrupted due to competitive crystallographic orientations. This effect is most pronounced at an Ar: N_2 ratio of 5:2, where the interference between Cr₂N (110) and CrN (200) growth directions leads to a highly disrupted columnar morphology. Notably, coatings deposited at this ratio also show superior surface characteristics, including higher density, smoother topography, and the lowest roughness (Ra = 0.256 nm). In contrast, coatings deposited at Ar: $N_2 = 3:1$ and 1:1 exhibit higher roughness values (Ra = 17.4 and 3.11 nm, respectively; see Fig. 3). The most distinct columnar structure is observed at Ar: $N_2 = 1:1$, corresponding to the formation of a single-phase CrN coating.

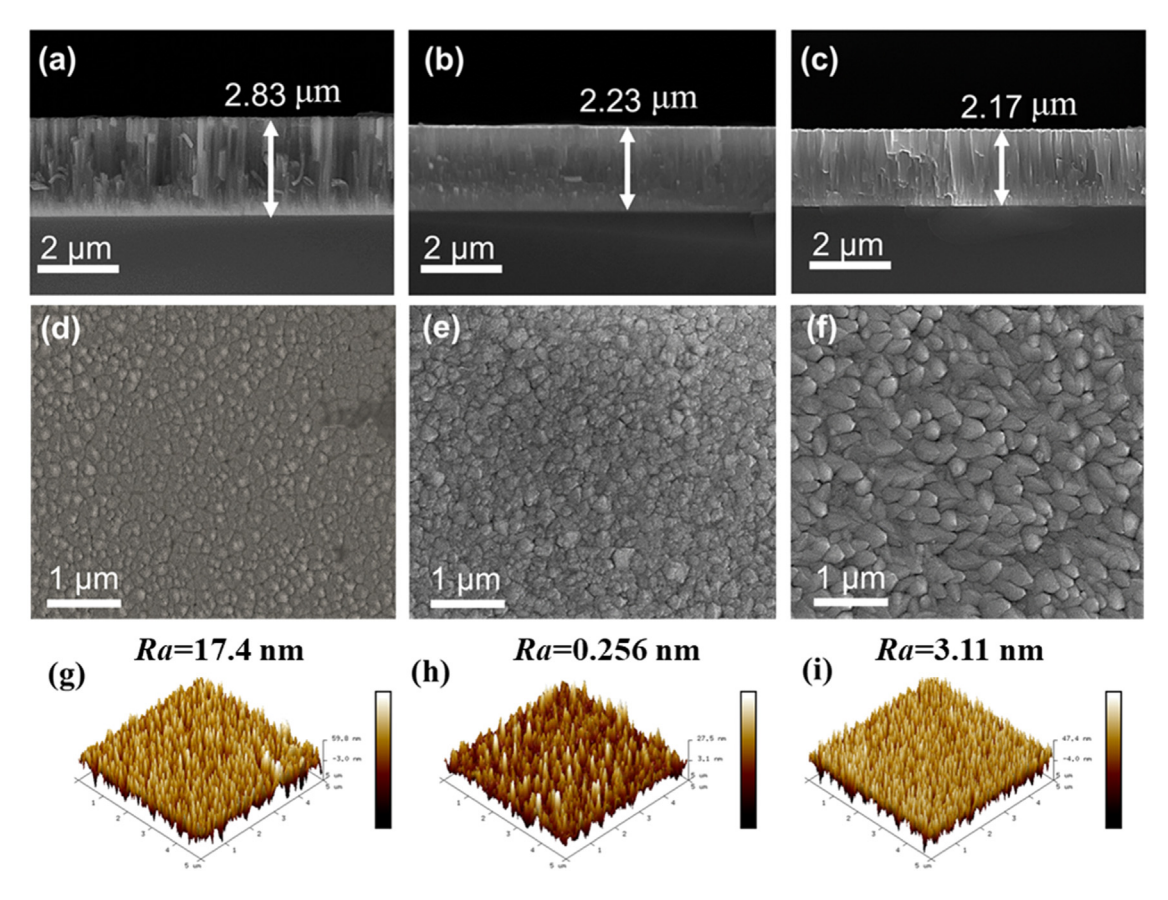


Fig. 3. (a-c) Cross-sectional, (d-f) surface morphologies images and (g-i) AFM diagrams of the as-deposited film: (a, d, g) $Ar:N_2 = 3:1$, (b, e, h) $Ar:N_2 = 5:2$, (c, f, i) $Ar:N_2 = 1:1$.

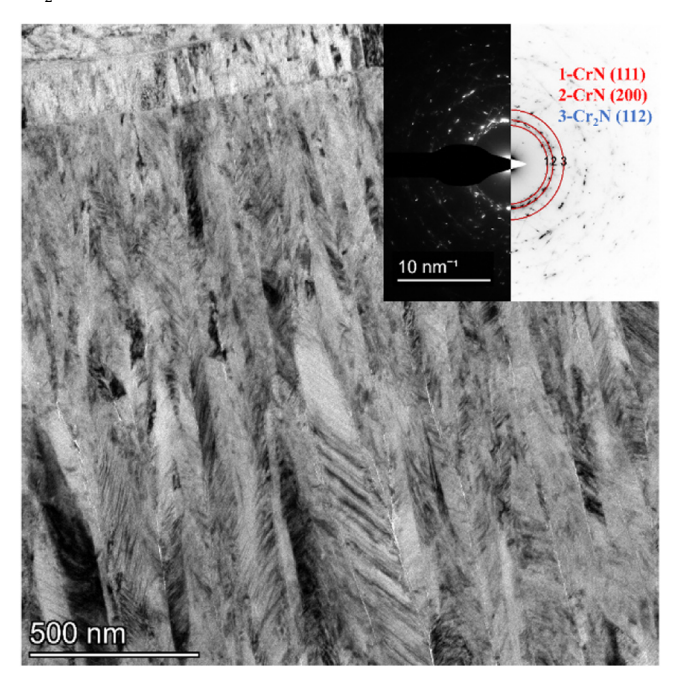


Fig. 4. Overview image and the corresponding SAED pattern of the Cr_xN with $Ar:N_2=5:2$.

3.2. Mechanical property

Fig. 6(a) presents the hardness and elastic modulus of the $Cr_{\chi}N$ with different Ar:N₂ (3:1, 5:2, 1:1). The coating hardness exhibits a non-monotonic trend with increasing N₂ flow rate, reaching a maxi-

mum value of 14.12 GPa at $Ar:N_2=5:2$, where the elastic modulus is minimized at 224.5 GPa. This increase in hardness is attributed to grain refinement in the dual-phase CrN/Cr_2N structure, as previously discussed.

According to the prior research, the H/E and H^3/E^2 ratios are indicative of a coating's resistance to plastic deformation [32]. Higher values of these ratios correspond to enhanced toughness and mechanical durability [33,34]. Krishnamurthy et al. [35] reported a good correlation between experimental results and simulated fracture toughness. At Ar:N $_2=5:2$, both H/E and H^3/E^2 are highest, confirming that the dual-phase CrN/Cr $_2$ N coating exhibits the best mechanical performance among the tested samples.

3.3. Electrochemical result

The passivation behavior is evident from the polarization curve shown in Fig. 7. In artificial seawater, the coating forms a passivation film primarily composed of Cr, N and O. The corrosion resistance of CrN coating is comparable to that of $\rm Cr_2O_3$ [36]. During tribological contact in a corrosive environment, the synergistic effect of friction and corrosion promotes the formation of this protective passive layer. However, mechanical abrasion during sliding continuously disrupts the film, allowing corrosive media to penetrate and interact with the underlying substrate. If the coating's wear resistance is sufficient to maintain the integrity of the passive layer under sliding conditions, material loss due to corrosion-assisted wear becomes minimal. Previous studies have shown that tribocorrosion-induced wear is negligible compared to purely mechanical wear mechanisms under similar loading conditions [37].

According to Fig. 7, the corrosion potential ($E_{\rm corr}$) and corrosion current density ($i_{\rm corr}$) of the sample were determined using the Tafel extrapolation method, with the results summarized in Table 2. The current density of the coating prepared with Ar:N₂ = 5:2 is an order of mag-

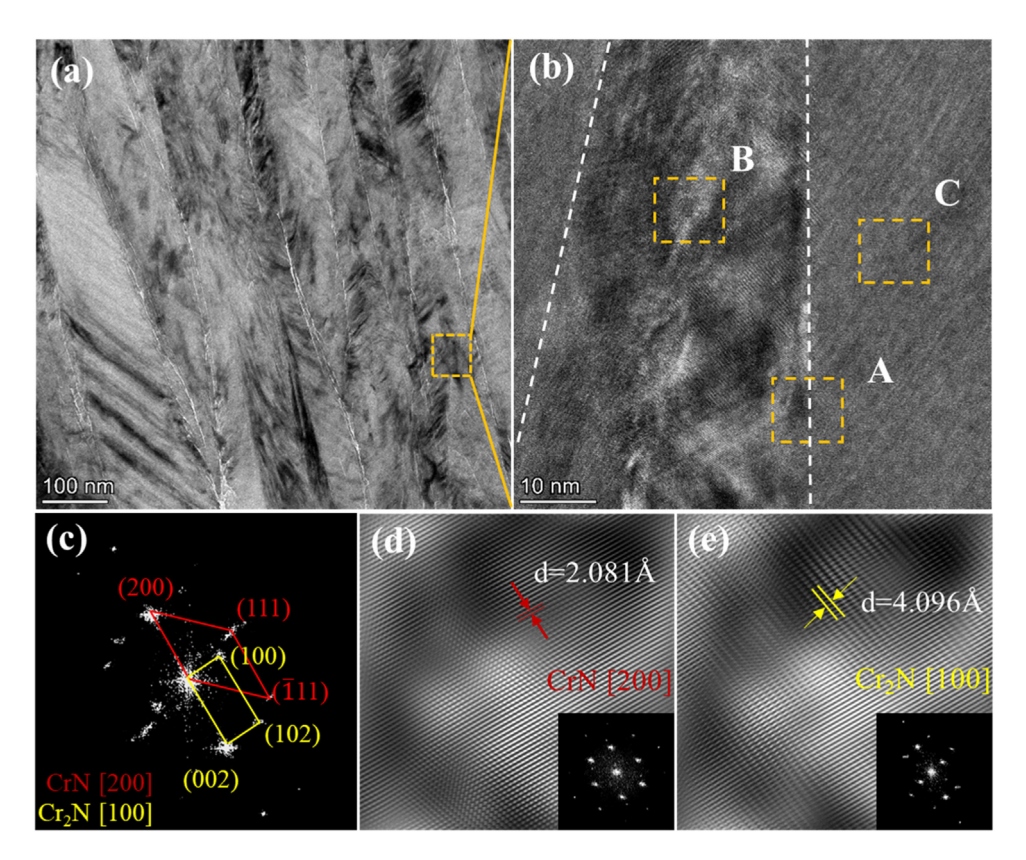


Fig. 5. (a) Cross-sectional TEM image and (b) high-resolution lattice image of phase border between hcp and fcc phase, (c) corresponding FFT diffraction pattern of area A in Fig. 5(b), inverse-FFT fringe image of areas (d) B and (e) C in Fig. 5(b).

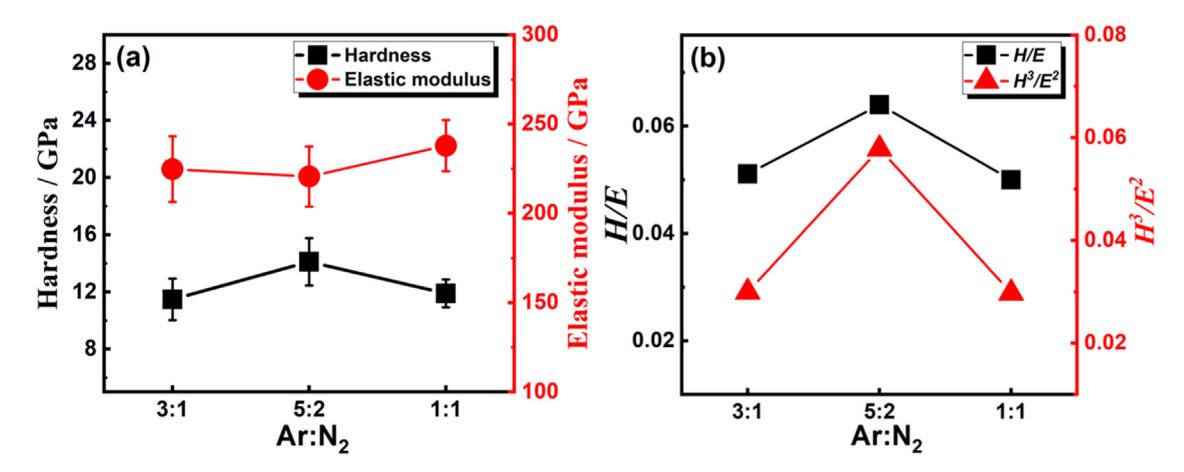


Fig. 6. (a) Variations of micro-hardness (H) and elastic modulus (E) of Cr_xN coatings deposited with different Ar: N_2 (3:1, 5:2, 1:1), (b) effects of Ar: N_2 (3:1, 5:2, 1:1) on H/E and H^3/E^2 ratio of Cr_xN coatings.

Table 2 $E_{\rm corr}$ and $i_{\rm corr}$ of ${\rm Cr_xN}$ coatings with different ${\rm Ar:N_2}$ ratios in the artificial seawater.

Sample	$E_{\rm corr}$ / V	i _{corr} /A•cm ⁻²
Ar:N ₂ = 3:1	-0.176	1.864×10^{-6}
$Ar:N_2 = 5:2$	-0.249	1.001×10^{-7}
$Ar:N_2 = 1:1$	-0.265	1.505×10^{-6}

nitude lower than that of the other two coatings, indicating superior corrosion resistance in the CrN–Cr $_2$ N dual-phase structure. Microscopic defects, pores, and columnar grains in the coating can serve as penetration pathways for corrosion electrolyte [21,38]. However, in the coating with Ar:N $_2$ = 5:2, the competitive growth between CrN and Cr $_2$ N phases

disrupts the development of a distinct columnar structure. Generally, coatings with a denser microstructure exhibit higher resistance to corrosive penetration [39]. Therefore, the compact structure and reduced defect density in the dual-phase coating effectively hinder the ingress of corrosive media. For comparison, the corrosion potential and current density of the uncoated 431 stainless steel are $-0.288\,\mathrm{V}$ and $2.06\times10^{-6}\,\mathrm{A/cm^2}$, respectively (Fig. S1(a)), demonstrating that the application of the coating significantly enhances corrosion performance.

3.4. Tribocorrosion result of Cr_xN coatings

The OCP over time due to sliding friction in artificial seawater for the three coatings is shown in Fig. 8(a). Under static conditions, passive materials exhibit stable, elevated OCP values. However, during sliding,

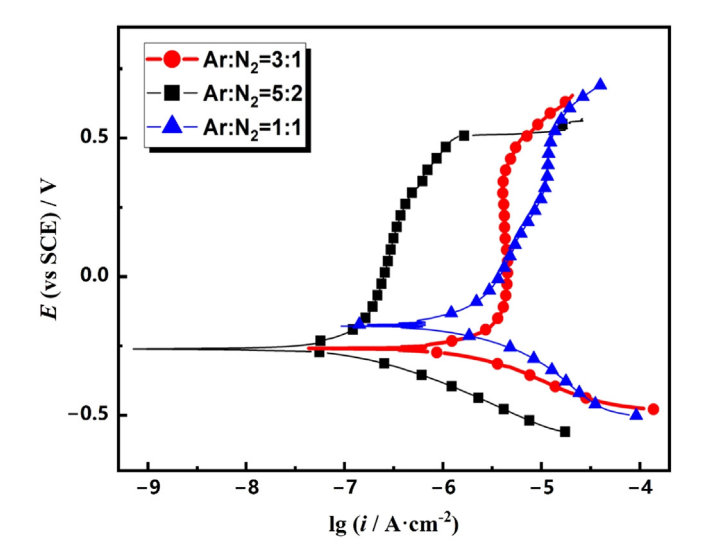


Fig. 7. Potentiodynamic polarization curves of Cr_xN coatings with different $Ar:N_2$ ratios in the artificial seawater.

the OCP shifts cathodically due to depassivation. The measured potential represents a mixed state, combining the active surface within the wear track and the passive regions outside it [40–43].

The steady-state OCP values prior to sliding were $-136~{\rm mV}$ (Ar:N $_2=3:1$), $-117~{\rm mV}$ (5:2), and $-146~{\rm mV}$ (1:1). Upon initiating sliding friction, all coatings exhibited an immediate cathodic shift, with OCPs dropping to $-302~{\rm mV}$ (3:1), $-349~{\rm mV}$ (5:2), and $-280~{\rm mV}$ (1:1). This sudden drop can be attributed to the removal of passive film and the increased exposure of the coating surface to the seawater environment [44,45]. During continued sliding, the OCP of all coatings stabilized quickly, indicating a dynamic balance between passive film removal and regeneration [46]. After sliding ceased, the OCP rose sharply and gradually returned to its initial steady-state value, reflecting the gradual re-passivation of newly exposed wear tracks.

The coating deposited at $Ar:N_2=5:2$ exhibited the highest OCP value prior to sliding and lowest during sliding, suggesting excellent initial corrosion resistance, but also a susceptibility to passive film breakdown under friction. This behavior may be attributed to the dual-phase composition of CrN and Cr_2N , where potential differences between phases could promote localized galvanic interactions, lowering OCP during wear. The OCP response of bare 431 stainless steel is provided in Fig. S1(b), confirming improved tribocorrosion resistance after coating deposition.

Fig. 8(b) shows the COF for the three coatings sliding against a $\rm Si_3N_4$ ball in seawater. For Ar:N₂ ratios of 3:1, 5:2 and 1:1, the COF initially

increased sharply before stabilizing at approximately 0.549, 0.50 and 0.628, respectively. The decrease in COF after the running-in period is attributed to increased contact smoothing due to wear, resulting in a more uniform friction interface. In addition, water in the environment provides hydrodynamic lubrication [45], and the lubricating film may act as a rolling medium, further smoothing the wear process [47].

The higher COF observed in the $Ar:N_2=1:1$ coating is attributed to its prominent columnar microstructure. The open grain boundaries inherent in this structure serve as pathways for corrosive media, undermining coating cohesion and promoting crack initiation and propagation during sliding [21]. The relationship between the average friction coefficient (based on three repeated tests per sample, with values averaged after 20 min of stabilization) and $Ar:N_2$ ratio is shown in Fig. 8(c), where the lowest COF was 0.54 observed for the coating prepared at $Ar:N_2=5:2$.

Fig. 9 shows the 3D surface morphology and 2D cross-sectional profiles of wear track on Cr_xN coatings after sliding in artificial seawater. The coating deposited at an $Ar:N_2$ ratio of 3:1 exhibits the highest wear rate among all samples, likely due to the synergistic effects of corrosion and mechanical wear in the saline environment. In this coating, the predominance of Cr and Cr_2N phases inhibits the formation of a stable Cr_2O_3 passive layer during sliding, rendering the surface more vulnerable to corrosive attack. Additionally, the relatively softer Cr phase, compared to Cr_2N/CrN , contributes to increased material removal, resulting in deeper wear tracks.

The coating deposited at $Ar:N_2=1:1$ also shows a relatively deep wear track, which can be attributed to its coarse columnar microstructure. This structural feature, characterized by a higher density of pinholes and grain boundaries, promotes the infiltration of corrosive media. Consequently, interfacial adhesion is weakened, and wear is accelerated through crack initiation and propagation [48].

In contrast, the coating produced at $Ar:N_2=5:2$, with its dual-phase (CrN/Cr₂N) structure, exhibits a denser microstructure (Fig. 3) that effectively resists crack propagation during sliding. This structural compactness contributes to improved wear resistance and enhanced tribocorrosion performance.

Fig. 10 illustrates the wear rates of $\mathrm{Cr_xN}$ coatings deposited under different $\mathrm{Ar:N_2}$ ratios. The coating deposited at $\mathrm{Ar:N_2}=3:1$ exhibits the highest wear rate. Artificial seawater, which contains a high concentration of chloride ions, aggressively attacks the coating surface through corrosion. During sliding, the rapid movement of the counterbody continuously removes the degraded surface layer, exposing fresh material to the corrosive environment. This exposure leads to anodic dissolution of the coating, thereby accelerating material loss. As wear progresses, more surface defects are generated, further promoting corrosion and exacerbating wear. Consequently, under the combined effects of corrosion and mechanical wear, the coatings deposited at $\mathrm{Ar:N_2}=3:1$ and 1:1 exhibit relatively higher wear rates.

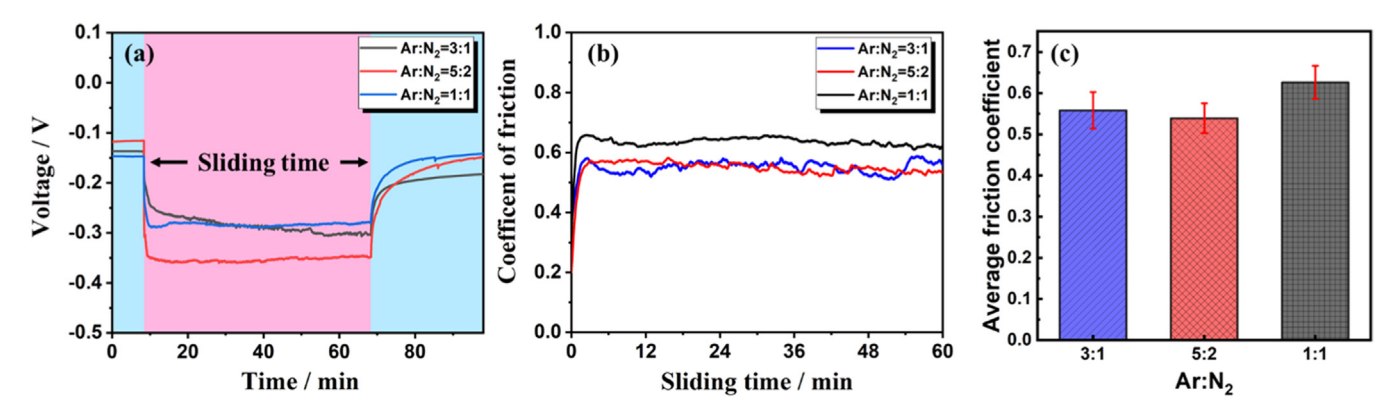


Fig. 8. (a) OCP, (b) COF-time value and (c) average value and standard deviation of the friction coefficient of Cr_vN coatings with different Ar:N₂ ratios.

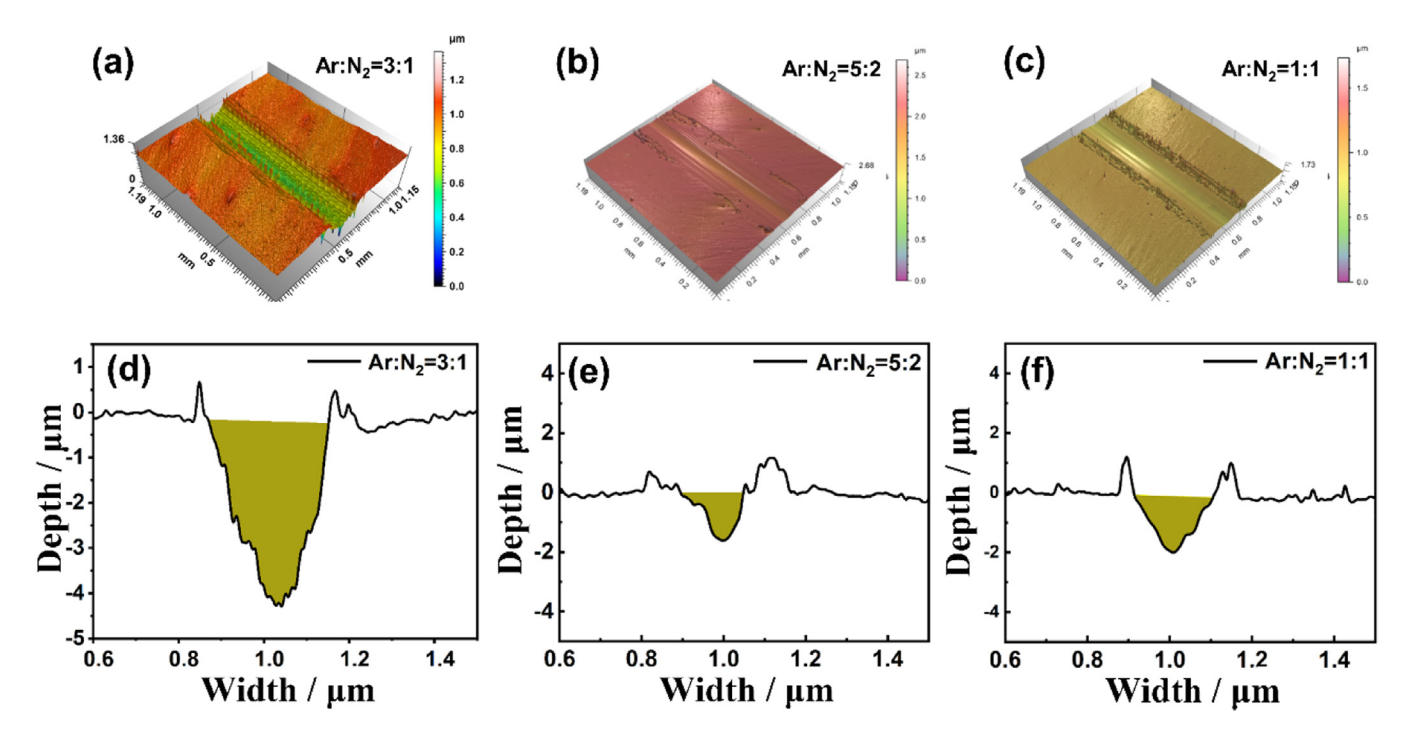


Fig. 9. (a-c) 3D cross-sectional and (d-f) cross profiles of the wear tacks: (a, d) $Ar:N_2 = 3:1$, (b, e) $Ar:N_2 = 5:2$, (c, f) $Ar:N_2 = 1:1$.

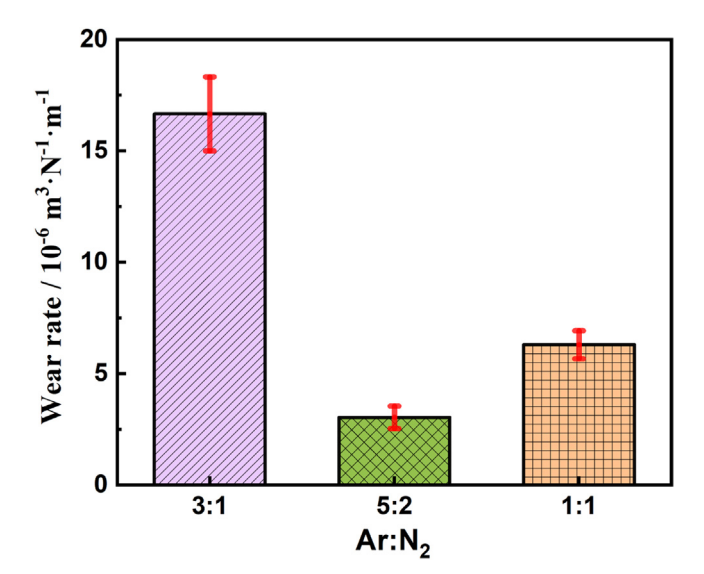


Fig. 10. Average wear rate of Cr_xN coatings with different $Ar:N_2$ ratios.

In contrast, the coating deposited at Ar:N $_2$ = 5:2 demonstrates the lowest wear rate. This coating features a dual-phase structure composed of CrN and Cr $_2$ N, with CrN exhibiting better oxidation resistance than Cr $_2$ N [49]. Importantly, the composite CrN–Cr $_2$ N system provides enhanced corrosion resistance compared to coatings composed of a single CrN or Cr $_2$ N phase [50]. Microstructural analysis (Fig. 3) further reveals that the coating deposited at Ar:N $_2$ = 5:2 has significantly higher density and lacks preferential grain orientation. These features contribute to improved barrier properties and enhanced resistance to both corrosion and tribological degradation [51].

Fig. 11 shows SEM images of the wear tracks on the $\rm Cr_x N$ coatings deposited under different $\rm Ar:N_2$ ratios. The width of the wear track is often used as an indicator of the coating's wear resistance, which is closely associated with both hardness and fracture toughness [52]. In the $\rm Ar:N_2=3:1$ coating, the presence of $\rm Cr$ and $\rm Cr_2 N$ phases contributes to brittle fracture and abrasive wear during sliding. The corresponding wear track measures 356 μm in width and shows significant abrasive debris accumulation (Fig. 11(a)). For the $\rm Ar:N_2=5:2$ coating, the wear track narrows to 308 μm and exhibits a smoother morphology with less evidence of abrasion (Fig. 11(b)). At $\rm Ar:N_2=1:1$, the wear track widens again to 346 μm and displays prominent parallel grooves and ploughing features typical of abrasive wear, but with minimal debris (Fig. 11(c)).

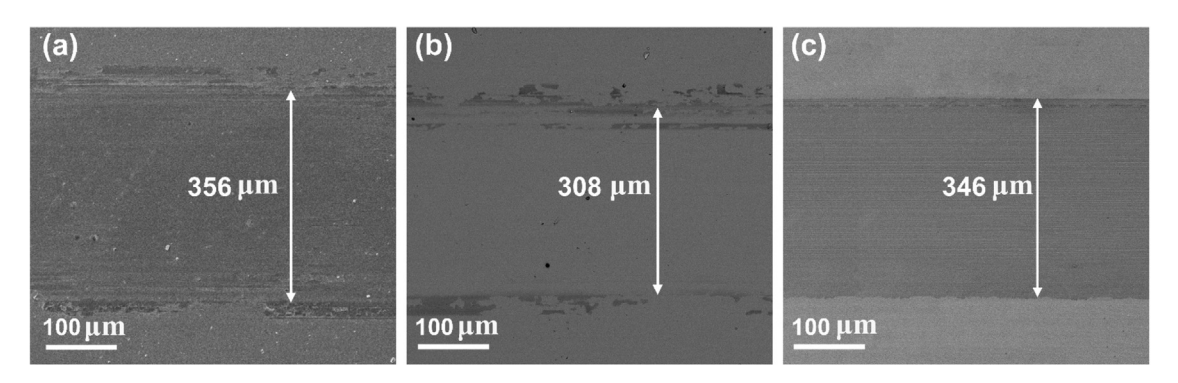


Fig. 11. SEM images of wear track of Cr_xN coatings with $Ar:N_2$ ratio (a) 3:1, (b) 5:2, (c) 1:1 after tribocorrosion test.

In summary, the dual-phase CrN and $\rm Cr_2N$ structure in the $\rm Ar: N_2 = 5:2$ coating enhances wear resistance, primarily due to improved resistance to brittle fracture enabled by the coexistence of both CrN and $\rm Cr_2N$ phases.

4. Conclusion

Three $\mathrm{Cr_xN}$ coatings with distinct structures were fabricated using the HiPIMS method by varying $\mathrm{Ar:N_2}$ gas ratios. Their microstructure, mechanical properties and tribocorrosion behavior in artificial seawater were systematically investigated. The study concludes that changes in the $\mathrm{Ar:N_2}$ ratio significantly influenced the phase composition of the coatings, thereby affecting their tribological and corrosion resistance. At an $\mathrm{Ar:N_2}$ ratio of 3:1, the coating was primarily composed of $\mathrm{Cr_2N}$. Increasing the ratio to 5:2 resulted in a mixed-phase structure of CrN and $\mathrm{Cr_2N}$, while a 1:1 ratio produced a near-pure CrN phase. Among the three, the coating deposited at an $\mathrm{Ar:N_2}$ ratio of 5:2 exhibited the best mechanical properties and corrosion resistance in artificial seawater. This improvement is attributed to the suppression of preferred orientation during the competitive growth of CrN and $\mathrm{Cr_2N}$, which disrupted the columnar structure and effectively hindered seawater penetration.

Data Availability Statement

The data used to support the findings of this study are available from the corresponding author upon request.

Declaration of competing interest

The authors declare that they have no known competing financial interests or personal relationships that could have appeared to influence the work reported in this paper.

CRediT authorship contribution statement

Xiaohui Zhou: Validation, Investigation, Methodology, Writing – original draft. Hong Du: Validation, Investigation, Methodology. Guanshui Ma: Methodology, Investigation. Zhenyu Wang: Methodology, Investigation. Wei Yang: Methodology, Investigation. Kazuhito Nishimura: Supervision, Funding acquisition. Peng Guo: Supervision, Funding acquisition. Aiying Wang: Writing – review & editing, Supervision, Funding acquisition. Peiling Ke: Supervision, Writing – review & editing, Funding acquisition.

Acknowledgements

This work was financially supported by the State Key Project of Fundamental Research of China (2022YFB3808802), National Science Fund for Distinguished Young Scholars of China (52025014), Natural Science Foundation of Ningbo (2022J305), Major Special Project of Ningbo (2023Z110, 2023Z198).

Supplementary materials

Supplementary material associated with this article can be found, in the online version, at doi:10.1016/j.corcom.2024.05.004.

References

- D. Landolt, S. Mischler, M. Stemp, Electrochemical methods in tribocorrosion: a critical appraisal, Electrochim. Acta 46 (2001) 3913–3929.
- [2] Y. Liu, A. Li, X. Cheng, S.Q. Zhang, H.M. Wang, Effects of heat treatment on microstructure and tensile properties of laser melting deposited AISI 431 martensitic stainless steel, Mater. Sci. Eng. A 666 (2016) 27–33.
- [3] V. Kumar, R. Penich, Stabilization of cubic phase in AlTiN coatings using anode configurations, Int. J. Refract. Met. Hard Mater. 60 (2016) 113–117.
- [4] M. Vorobyova, F. Biffoli, W. Giurlani, S.M. Martinuzzi, M. Linser, A. Caneschi, M. Innocenti, PVD for decorative applications: a review, Materials 16 (2023) 4919.
- [5] O. Durst, J. Ellermeier, C. Berger, Influence of plasma-nitriding and surface roughness on the wear and corrosion resistance of thin films (PVD/PECVD), Surf. Coat. Technol. 203 (2008) 848–854.

- [6] Y.L. Su, J.S. Lin, An investigation of the tribological potential of TiN, CrN and TiN+ CrN physical vapor deposited coatings in machine element applications, Wear 170 (1993) 45–53.
- [7] C. Gautier, H. Moussaoui, F. Elstner, J. Machet, Comparative study of mechanical and structural properties of CrN films deposited by d.c. magnetron sputtering and vacuum arc evaporation, Surf. Coat. Technol. 86–87 (1996) 254–262.
- [8] J.H. Xu, H. Umehara H, I. Kojima, Effect of deposition parameters on composition, structures, density and topography of CrN films deposited by r.f. magnetron sputtering, Appl. Surf. Sci. 201 (2002) 208–218.
- [9] J. Lin, Z.L. Wu, X.H. Zhang, B. Mishra, J.J. Moore, W.D. Sproul, A comparative study of CrN_x coatings synthesized by dc and pulsed dc magnetron sputtering, Thin Solid Films 517 (2009) 1887–1894.
- [10] P.H. Mayrhofer, H. Willmann, C. Mitterer, Oxidation kinetics of sputtered Cr-N hard coatings, Surf. Coat. Technol. 146 (2001) 222–228.
- [11] G. Wei, T.W. Scharf, J.N. Zhou, F. Huang, M.L. Weaver, J.A. Barnard, Nanotribology studies of Cr, Cr₂N and CrN thin films using constant and ramped load nanoscratch techniques, Surf. Coat. Technol. 146 (2001) 357–362.
- [12] V.K.W. Grips, H.C. Barshilia, V.E. Selvi, K.S.R. Kalavati, Electrochemical behavior of single layer CrN, TiN, TiAIN coatings and nanolayered TiAIN/CrN multilayer coatings prepared by reactive direct current magnetron sputtering, Thin Solid Films 514 (2006) 204–211.
- [13] Z. Fei, W. Yuan, L. Feng, Y. Meng, Z.J.W. Dai, Friction and wear properties of duplex MAO/CrN coatings sliding against Si₃N₄ ceramic balls in air, water and oil, Wear 267 (2009) 1581–1588.
- [14] J.L. Lin, J.J. Moore, W.D. Sproul, B. Mishra, Z.L. Wu, J. Wang, The structure and properties of chromium nitride coatings deposited using dc, pulsed dc and modulated pulse power magnetron sputtering, Surf. Coat. Technol. 204 (2010) 2230– 2230
- [15] H. Bai, J. Li, J. Gao, J. Ni, Y. Bai, J. Jian, L. Zhao, B. Bai, Z. Cai, J. He, H. Chen, X. Leng, X. Liu, Comparison of CrN coatings prepared using high-power impulse magnetron sputtering and direct current magnetron sputtering, Materials 16 (2023) 1–21.
- [16] D.E. Tranca, A. Sobetkii, R. Hristu, S.R. Anton, E. Vasile, S.G. Stanciu, C.K. Banica, E. Fiorentis, D. Constantinescu, G.A. Stanciu, Structural and mechanical properties of CrN thin films deposited on Si substrate by using magnetron techniques, Coatings 13 (2023) 1–15.
- [17] H. Zhang, S.W. Duo, X.M. Xu, T.Z. Liu, Effect of N₂ flow rate on structure and mechanical properties of CrN coatings prepared by closed field unbalanced magnetron sputtering, Key Eng. Mater. 591 (2014) 95–98.
- [18] Q. Chen, H. Yang, L. Wu, X. Wu, C. Zhu, L. He, N. Liu, Y. Yang, J. Liao, J. Yang, Effect of the Ar/N₂ flow ratio on the microstructure, mechanical properties, and high-temperature steam oxidation behavior of Cr/Cr_xN coatings for accident-tolerant fuel coatings, Corros. Sci. 192 (2021) 109833.
- [19] J.L. Lin, W.D. Sproul, J.J. Moore, S. Lee, S. Myers, High rate deposition of thick CrN and Cr₂N coatings using modulated pulse power (MPP) magnetron sputtering, Surf. Coat. Technol. 205 (2011) 3226–3234.
- [20] P. Hones, R. Sanjines, F. Levy, Characterization of sputter-deposited chromium nitride thin films for hard coatings, Surf. Coat. Technol. 94-95 (1997) 398–402.
- [21] L. Shan L, Y. Wang, J. Li, J. Chen, Effect of N₂ flow rate on microstructure and mechanical properties of PVD CrN_x coatings for tribological application in seawater, Surf. Coat. Technol. 242 (2014) 74–82.
- [22] Standard ASTM D1141-98, Standard practice for preparation of substitute ocean water, American Society for Testing and Materials (2021).
- [23] Y. Liu, S. Li, X. Zhou, P. Guo, R. Chen, J. Wei, A.Y. Wang, P.L. Ke, Enhanced anti-tribocorrosion property of a-C film under high hydrostatic pressure by high power pulsed magnetron sputter (HiPIMS), J. Mater. Res. Technol. 28 (2024) 3052– 3067.
- [24] Q.H. Kong, L. Ji, H.X. Li, X.H. Liu, Y.J. Wang, J.M. Chen, H.D. Zhou, Composition, microstructure, and properties of CrN_x films deposited using medium frequency magnetron sputtering, Appl. Surf. Sci. 257 (2011) 2269–2274.
- [25] A. Conde, A.B. Cristobal, G. Fuentes, T. Tate, J. Damborenea, Surface analysis of electrochemically stripped CrN coatings, Surf. Coat. Technol. 201 (2006) 3588–3595.
- [26] S.H. Zhang, M.X. Li, Y.Z. He, T. Cho, H.G. Chun, J. Yoon, S.H. Si, H.S. Li, Synthesis and properties of CrN_x/amorphous-WC nanocomposites prepared using hybrid arc ion plating and direct current magnetron sputtering, Thin Solid Films 519 (2010) 751–758.
- [27] S.H. Zhang, J.L. Li, Z. Chen, M.X. Li, Realization of superhard chromium nitride-based films: a superlattice nanocrystalline-Cr₂N/amorphous-WC film, Thin Solid Films 520 (2012) 4984–4989.
- [28] A. Lippitz, T. Hubert, XPS investigations of chromium nitride thin films, Surf. Coat. Technol. 200 (2005) 250–253.
- [29] S.F. Zhu, L. Chen, Y.P. Wu, Y. Hu, T.W. Liu, K. Tang, Q. Wei, Microstructure and corrosion resistance of Cr/Cr₂N multilayer film deposited on the surface of depleted uranium, Corros. Sci. 82 (2014) 420–425.
- [30] T. Hurkmans, D.B. Lewis, J.S. Brooks, W.D. Mvnz, Chromium nitride coatings grown by unbalanced magnetron (UBM) and combined arc/unbalanced magnetron (ABSTM) deposition techniques, Surf. Coat. Technol. 86–87 (1996) 192–199.
- [31] M. Novakovic, M. Popovic, Z. Rakocevic, N. Bibic, Structural, optical and electrical properties of reactively sputtered Cr_xN_y films: nitrogen influence on the phase formation, Process. Appl. Ceram. 11 (2017) 45–51.
- [32] J. Musil, Hard nanocomposite films prepared by reactive magnetron sputtering, in: A.A. Voevodin, D.V. Shtansky, E.A. Levashov, J.J. Moore (Eds.), Nanostructured Thin Films and Nanodispersion Strengthened Coatings. NATO Science Series II: Mathematics, Physics and Chemistry, Berlin, Springer, vol. 155, 2004, 43–56.
- [33] X.J. Chen, Y. Du, Y.W. Chung, Commentary on using H/E and H³/E² as proxies for fracture toughness of hard coatings, Thin Solid Films 688 (2019) 137265.

- [34] A. Leyland, A. Matthews, On the significance of the H/E ratio in wear control: a nanocomposite coating approach to optimised tribological behaviour, Wear 246 (2000) 1–11.
- [35] S. Krishnamurthy, I.E. Reimanis, J. Berger, F. Drexler, Fracture toughness measurement of chromium nitride films on brass, J. Am. Ceram. Soc. 87 (2004) 1306–1313.
- [36] C.H. Hsu, C.Y. Lee, K.L. Chen, J.H. Lu, Effects of CrN/EN and Cr₂O₃/EN duplex coatings on corrosion resistance of ADI, Thin Solid Films 517 (2009) 5248–5252.
- [37] R. Priya, C. Mallika, U.K. Mudali, Wear and tribocorrosion behaviour of 304L SS, Zr-702, Zircaloy-4 and Ti-grade2, Wear 310 (2014) 90–100.
- [38] Y.R. Liu, H. Du, X. Zuo, P. Guo, L. Liu, K.R. Lee, A.Y. Wang, P.L. Ke, Cr/GLC multilayered coating in simulated deep-sea environment: corrosion behavior and growth defect evolution, Corros. Sci. 188 (2021) 109528.
- [39] J.L. Lin, W.D. Sproul, J.J. Moore, S. Lee, S. Myers, High rate deposition of thick CrN and Cr₂N coatings using modulated pulse power (MPP) magnetron sputtering, Surf. Coat. Technol. 205 (2011) 3226–3234.
- [40] M. Azzi, M. Paquette, J.A. Szpunar, J.E. Klemberg-Sapieha, L. Martinu, Tribocorrosion behaviour of DLC-coated 316L stainless steel, Wear 267 (2009) 860–866.
- [41] L. Benea, V.E. Iordache, F. Wenger, P. Ponthiaux, J. Vallory, Tribocorrosion mechanism study of satellite-6 and zircaloy-4-A comparison in LIOH- H3B03 solutions, Ann. Univ. "DUNĂR EA JOS" GALAŢI 8 (2005) 35–40.
- [42] A. Berradja, F. Bratu, L. Benea, G. Willems, J.P. Celis, Effect of sliding wear on tribocorrosion behaviour of stainless steels in a Ringer's solution, Wear 261 (2006) 987–993
- [43] J. Perret, E. Boehm-Courjault, M. Cantoni, S. Mischler, A. Beaudouin, W. Chitty, J.P. Vernot, EBSD, SEM and FIB characterisation of subsurface deformation during tribocorrosion of stainless steel in sulphuric acid, Wear 269 (2010) 383–393.

- [44] A. Hatem, J.L. Lin, R.H. Wei, R.D. Torres, C. Laurindo, G.B. Souza, P. Soares, Tribocorrosion behavior of low friction TiSiCN nanocomposite coatings deposited on titanium alloy for biomedical applications. Surf. Coat. Technol. 347 (2018) 1–12.
- [45] J.R. Roos, J.P. Celis, E. Vancoille, H. Veltrop, S. Boelens, F. Jungblut, J. Ebberink, H. Homberg, Interrelationship between processing, coatingproperties and functional properties of steered arc physically vapour deposited (Ti,AI)N and (Ti,Nb)N coatings, Thin Solid Films 193–194 (1990) 547–556.
- [46] Y.W. Ye, Y.X. Wang, X.L. Ma, D.W. Zhang, L.P. Wang, X.G. Li, Tribocorrosion behaviors of multilayer PVD DLC coated 304L stainless steel in seawater, Diam. Relat. Mater. 79 (2017) 70–78.
- [47] A. Neville, A. Morina, T. Haque, M. Voong, Compatibility between tribological surfaces and lubricant additives—How friction and wear reduction can be controlled by surface/lube synergies, Tribol. Int. 40 (2007) 1680–1695.
- [48] C. Liu, A. Leyland, Q. Bi, A. Matthews, Corrosion resistance of multi-layered plasma-assisted physical vapour deposition TiN and CrN coatings, Surf. Coat. Technol. 141 (2001) 164–173.
- [49] Z.B. Qi, B. Liu, Z.T. Wu, F.P. Zhu, Z.C. Wang, C.H. Wu, A comparative study of the oxidation behavior of $\rm Cr_2N$ and $\rm CrN$ coatings, Thin Solid Films 544 (2013) 515–520.
- [50] I.E. Paulauskas, M.P. Brady, H. Iii, R.A. Buchanan, L.R. Walker, Corrosion behavior of CrN, Cr₂N and π phase surfaces on nitrided Ni–50Cr for proton exchange membrane fuel cell bipolar plates, Corros. Sci. 48 (2006) 3157–3171.
- [51] F.S. Shieu, Y.C. Sung, L.H. Cheng, J.H. Huang, G.P. Yu, Control of the corrosion resistance of TiN-coated AISI 304 stainless steel, Corros. Sci. 39 (1997) 893– 899.
- [52] J. Musil, Hard nanocomposite coatings: thermal stability, oxidation resistance and toughness, Surf. Coat. Technol. 207 (2012) 50–65.